PHYSICAL REVIEW B **93**, 045311 (2016)

Cross-plane thermal conductivity of (Ti,W)N/(Al,Sc)N metal/semiconductor superlattices

Bivas Saha,[1,4,*,†] Yee Rui Koh,[2,4,†] Jonathan Comparan,[1,4] Sridhar Sadasivam,[3,4] Jeremy L. Schroeder,[5] Magnus Garbrecht,[5]
Amr Mohammed,[2,4] Jens Birch,[5] Timothy Fisher,[3,4] Ali Shakouri,[2,4] and Timothy D. Sands[6]
[1]*School of Materials Engineering, Purdue University, West Lafayette, Indiana 47907, USA*
[2]*School of Electrical and Computer Engineering, Purdue University, West Lafayette, Indiana 47907, USA*
[3]*School of Mechanical Engineering, Purdue University, West Lafayette, Indiana 47907, USA*
[4]*Birck Nanotechnology Center, Purdue University, West Lafayette, Indiana 47907, USA*
[5]*Thin Film Physics Division, Department of Physics, Chemistry, and Biology (IFM), Linköping University, SE-581 83 Linköping, Sweden*
[6]*Bradley Department of Electrical and Computer Engineering and Department of Materials Science and Engineering, Virginia Tech, Blacksburg, Virginia 24061, USA*

(Received 26 February 2015; revised manuscript received 10 September 2015; published 21 January 2016)

Reduction of cross-plane thermal conductivity and understanding of the mechanisms of heat transport in nanostructured metal/semiconductor superlattices are crucial for their potential applications in thermoelectric and thermionic energy conversion devices, thermal management systems, and thermal barrier coatings. We have developed epitaxial (Ti,W)N/(Al,Sc)N metal/semiconductor superlattices with periodicity ranging from 1 nm to 240 nm that show significantly lower thermal conductivity compared to the parent TiN/(Al,Sc)N superlattice system. The (Ti,W)N/(Al,Sc)N superlattices grow with [001] orientation on the MgO(001) substrates with well-defined coherent layers and are nominally single crystalline with low densities of extended defects. Cross-plane thermal conductivity (measured by time-domain thermoreflectance) decreases with an increase in the superlattice interface density in a manner that is consistent with incoherent phonon boundary scattering. Thermal conductivity values saturate at 1.7 $\mathrm{W\,m^{-1}\,K^{-1}}$ for short superlattice periods possibly due to a delicate balance between long-wavelength coherent phonon modes and incoherent phonon scattering from heavy tungsten atomic sites and superlattice interfaces. First-principles density functional perturbation theory based calculations are performed to model the vibrational spectrum of the individual component materials, and transport models are used to explain the interface thermal conductance across the (Ti,W)N/(Al,Sc)N interfaces as a function of periodicity. The long-wavelength coherent phonon modes are expected to play a dominant role in the thermal transport properties of the short-period superlattices. Our analysis of the thermal transport properties of (Ti,W)N/(Al,Sc)N metal/semiconductor superlattices addresses fundamental questions about heat transport in multilayer materials.

DOI: 10.1103/PhysRevB.93.045311

I. INTRODUCTION

Thermal transport in superlattice metamaterials has attracted significant interest [1–3] in recent years due to the ability of superlattice metamaterials to serve as model systems where advanced theoretical concepts of heat conduction [4,5] can be demonstrated and verified. A detailed understanding of the various heat transport mechanisms in superlattices is crucial for designing advanced thermoelectric and thermionic energy conversion devices [6,7] as well as thermal barrier coatings [8] with improved efficiencies. Heat conduction in superlattices can be engineered through mechanisms such as acoustic impedance mismatch [9–12], boundary resistance at the interfaces [13], alloy scattering [9–11], phonon miniband formation [12], phonon tunneling [14], and coherent phonon heat transport [4–5,15]. In the case of thermoelectric applications, it is generally necessary for the cross-plane thermal conductivity of the superlattices to be below about 1 $\mathrm{W\,m^{-1}\,K^{-1}}$ at the operating temperatures.

Theoretical models [16,17] have predicted that epitaxial metal/semiconductor superlattices with optimized Schottky barrier heights and low cross-plane thermal conductivities should exhibit high thermoelectric figure-of-merit (ZT) values at high operating temperatures. Most of the studies of heat transport mechanisms in superlattices employ semiconductor/semiconductor superlattices [11,18]. There are a few reports on thermal transport in metal/semiconductor superlattices, specifically epitaxial ZrN/ScN [19,20] and HfN/ScN [21] superlattice systems.

We recently developed an epitaxial, single crystalline TiN/(Al,Sc)N metal/semiconductor superlattice [22–24] system that can be free of extended defects in a relaxed or nearly relaxed state. We analyzed the cross-plane thermal properties of these superlattices and observed an incoherent to long-wavelength coherent phonon regime transition (see Ref. [25]). The superlattices also exhibited extremely high interface thermal conductances (ITCs) due to the dominance of long-wavelength coherent phonon modes that do not see superlattice interfaces and that travel ballistically across the superlattice. While the observation of such coherent phonon modes in thermal transport across TiN/(Al,Sc)N superlattices was notable, the room temperature thermal conductivity of the superlattices varied between 4.5 to 9 $\mathrm{W\,m^{-1}\,K^{-1}}$ depending on the period thickness, which is too high for practical thermoelectric applications. In this report, we present results on the reduction of cross-plane thermal conductivity through

---

[*] Present address: Department of Materials Science and Engineering, University of California at Berkeley, Berkeley, CA 94720, USA; bsaha@berkeley.edu

[†] These authors have contributed equally in this work.

heavy element alloying effects that result in room temperature thermal conductivity values as low as 1.7 W m^{-1} K^{-1}. We alloy tungsten nitride (WN) with TiN to grow $Ti_{0.7}W_{0.3}N$ metallic alloys and to develop epitaxial $Ti_{0.7}W_{0.3}N/Al_{0.72}Sc_{0.28}N$ metal/semiconductor superlattices on 001-oriented MgO substrates. Tungsten atoms help reduce the thermal conductivity by decreasing phonon group velocities and by acting as scattering centers for short-wavelength phonons. Incoherent phonon scattering with tungsten atoms also ensures that heat transport in short-period superlattices is not dominated by long-wavelength coherent phonons. The observed thermal conductivity reduction in epitaxial $Ti_{0.7}W_{0.3}N/Al_{0.72}Sc_{0.28}N$ metal/semiconductor superlattices warrants further research on their electrical properties to explore their applications in high temperature thermoelectric and thermionic devices.

We use a reactive dc-magnetron sputtering with a high vacuum chamber to deposit the thin-film and superlattice samples. A detailed discussion of the growth procedure is presented in the experimental method section of the Supplemental Material [26] as well as in Refs. [22] and [23].

II. STRUCTURAL CHARACTERIZATION

A. X-ray diffraction

Symmetric 2θ-ω x-ray diffraction (XRD) patterns of $Ti_{0.7}W_{0.3}N/Al_{0.72}Sc_{0.28}N$ superlattices [Fig. 1(a)] exhibit a series of diffraction peaks, characteristic of periodic superlattices as well as the split (see Supplemental Material [26] for more details) 002 MgO substrate peak. The strongest peaks, denoted by 002 S/L in Fig. 1(a), are characteristic of the average lattice parameter of the superlattice layers and appear at 42.15° and 41.9° for the superlattices having nominal period thicknesses of 20 nm and 10 nm, respectively. This corresponds to [001]-oriented growth with average lattice parameters of 4.28 Å and 4.31 Å for these superlattices with nominal $Ti_{0.7}W_{0.3}N/Al_{0.72}Sc_{0.28}N$ layer thicknesses 10 nm/10 nm and 5 nm/5 nm, respectively. The main 002-diffraction peak and the satellites for the superlattice having 40 nm period thickness split into doublets [see Fig. 1(a)] with the peaks separated by 0.1°. We suspect that such splitting of the diffraction peaks is due to separate superlattice domains that are spatially separated from each other having relaxed to different degrees. The XRD results indicate that the superlattices are comprised of cubic

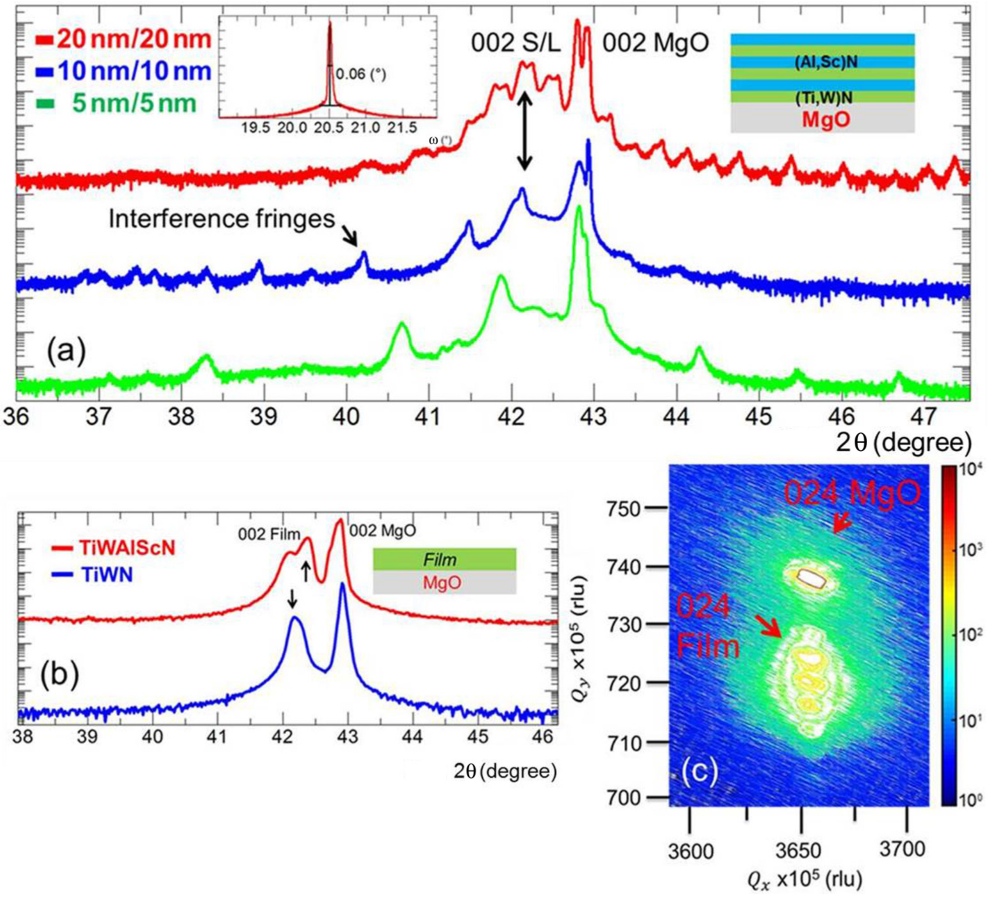

FIG. 1. (a) Symmetric 2θ-ω x-ray diffractograms of $Ti_{0.7}W_{0.3}N/Al_{0.72}Sc_{0.28}N$ superlattices with nominal period thicknesses of 10 nm, 20 nm, and 40 nm. Superlattices grow [001]-oriented on MgO(001) substrates. Superlattice satellites are clearly visible in the diffractograms. Inset shows rocking curve FWHM of a 20 nm period superlattice. (b) The XRD patterns of $Ti_{0.7}W_{0.3}N$ and $Ti_{0.35}W_{0.15}Al_{0.36}Sc_{0.14}N$ thin film alloys grown on 001 MgO substrates. (c) X-ray reciprocal space map of a 20 nm/20 nm superlattice. The main 024-diffraction peak, the MgO 024 peak, and the interference fringes are all aligned vertically, which suggests epitaxial and pseudomorphic superlattice growth with respect to the MgO substrate.

[001]-oriented $Al_{0.72}Sc_{0.28}N$ (see Ref. [22]) and $Ti_{0.7}W_{0.3}N$ (see Refs. [27] and [28]) individual layers isostructurally grown onto the MgO(001) substrates.

The clearly visible superlattice satellites [see Fig. 1(a)] are characteristic of the periodic arrangement of the individual layers and show that both the thicknesses and the crystalline lattices in the individual layers are well defined throughout the films. However, we note that not every one of the second order satellites is extinct in the superlattices (especially in the nominal 5 nm/5 nm and 20 nm/20 nm superlattice samples), which indicates a small degree of layer thickness variation, suggesting that the individual layer thicknesses are not exactly half of the period thickness values, as originally intended. Careful observations of Fig. 1(a) also show that the satellites are asymmetric in shape, which is due to small layer thickness variations within a particular superlattice. Since the sputter deposition rate usually varies slightly with respect to the sputter time and other stochastic variables, the small changes in thicknesses are not surprising. The superlattices exhibit a small degree of mosaicity, as evidenced by the small rocking curve full-width-at-half-maximum (FWHM) values of the 002-diffraction peak (0.03° for 5 nm/5 nm, 0.06° for 10 nm/10 nm, and 0.07° for 20 nm/20 nm superlattices). Such small rocking curve FWHM values suggest that the superlattices are nominally single crystalline with low densities of extended defects.

The $Ti_{0.7}W_{0.3}N$ and $Ti_{0.35}W_{0.15}Al_{0.36}Sc_{0.14}N$ alloys also show [001]-oriented growth on MgO(001) substrates [Fig. 1(b)]. The measured out-of-plane lattice constant for $Ti_{0.7}W_{0.3}N$ ($c = 4.28$ Å) represents the average c-axis lattice constant of bulk TiN ($c = 4.24$ Å) and WN ($c = 4.31$ Å) [27]. The $Ti_{0.35}W_{0.15}Al_{0.36}Sc_{0.14}N$ alloy has a lattice constant of $c = 4.26$ Å (corresponding to the highest intensity peak) and the small rocking curve FWHM value of 0.08° that indicates excellent crystal quality. The main 002-diffraction peak of the $Ti_{0.35}W_{0.15}Al_{0.36}Sc_{0.14}N$ alloy splits into two [see Fig. 1(b)]. While we have been unable to verify the exact origin of the peak splitting, we suspect that it is due to the phase separation of component materials in the alloy. Both AlN and δ-WN crystallize in the hexagonal wurtzite structure under ambient conditions. And though β-W_2N has a cubic (B1) crystal structure, it has a wide composition range [27] from $WN_{0.43}$ to $WN_{0.72}$ at temperatures above 280 °C. Therefore, it is possible that one or more of the parent nitride materials might have phase separated to a small degree resulting in the splitting of the main 002-diffraction peak. To properly address this question, further transmission electron microscopy (TEM) based analyses are required, which is beyond the scope of the present paper.

We obtained an XRD reciprocal space map (RSM) of a 20 nm/20 nm $Ti_{0.7}W_{0.3}N/Al_{0.72}Sc_{0.28}N$ superlattice [Fig. 1(c)] to gain further information about its crystal structure. The RSM shows vertical alignment of the main 024 MgO peak, 024-superlattice peak, and superlattice satellites, which means that the superlattice is pseudomorphic with respect to the MgO substrate. Thus, since the lattice constant of MgO ($a = 4.21$ Å) is smaller than the relaxed lattice constants of both $Ti_{0.7}W_{0.3}N$ and $Al_{0.72}Sc_{0.28}N$, the in-plane lattice constants (a) of both individual layers are compressively strained by the in-plane fixation to the substrate, accompanied by a slight expansion in the lattice constants of the component materials along the cross-plane growth direction (c).

B. Electron microscopy characterization

Microstructural details of the superlattices were analyzed by high-resolution transmission electron microscopy (HRTEM) and high-angle annular dark-field scanning transmission electron microscopy (HAADF-STEM) studies on a 5 nm/5 nm $Ti_{0.7}W_{0.3}N/Al_{0.72}Sc_{0.28}N$ superlattice. The low-magnification TEM micrographs in Figs. 2(a) and 2(b) clearly show distinct individual $Ti_{0.7}W_{0.3}N$ and $Al_{0.72}Sc_{0.28}N$ layers separated by sharp and abrupt interfaces. The high-magnification image in Fig. 2(c) suggests cubic epitaxial crystal growth with an orientation relationship of $Ti_{0.7}W_{0.3}N$(001)[100]|| MgO (001)[100] and $Al_{0.72}Sc_{0.28}N$ (001)[100]||$Ti_{0.7}W_{0.3}N$ (001)[100]. It is clear from Fig. 2(c) that the individual layer thicknesses of $Ti_{0.7}W_{0.3}N$ and $Al_{0.72}Sc_{0.28}N$ are not exactly half of the period thickness values, which correlates well with our XRD analysis where we see all orders of satellites. The $Al_{0.72}Sc_{0.28}N$ layer thickness is seen to be larger than the $Ti_{0.7}W_{0.3}N$ layer thickness for this particular superlattice. Fast Fourier transforms (FFTs) of each of the layers presented in Figs. 2(d) and 2(e) show cubic intensity patterns with identical lattice spacings. The low-magnification HAADF-STEM micrograph in Fig. 3(a) shows sharp superlattice interfaces, and high-resolution HAADF-STEM images [Fig. 3(b)] show the lattice fringes (in the inset) that confirm the high crystalline quality at the interfaces and within the layers. Our microscopy analyses also show some interfacial dislocations; however, we have been unable to identify their origin and role in relieving misfit strain, if any.

III. THERMAL CONDUCTION

A. Room temperature measurements

The cross-plane thermal conductivity of the individual films and the superlattices are measured with a time domain thermoreflectance (TDTR) measurement system. A detailed description of the measurement technique and data fitting are presented in the Supplemental Material [26]. We use a 70 nm thick aluminum (Al) layer (deposited via thermal evaporation) as the transducer for all of our TDTR measurements. Two different frequencies (6 MHz and 9 MHz) are used to measure the thermal conductivity of each sample, and the values match within 5% accuracy. The samples analyzed in this paper have a total thickness of approximately 240 nm.

The room temperature thermal conductivity of the $Ti_{0.7}W_{0.3}N$ alloy is $6.4\ \mathrm{W\,m^{-1}\,K^{-1}}$ (Fig. 4), while the electronic contribution to thermal conductivity is calculated to be $2.1\ \mathrm{W\,m^{-1}\,K^{-1}}$ using the Wiedemann-Franz law and a measured in-plane electrical conductivity of $2.8 \times 10^5\ \mathrm{S\,m^{-1}}$. The lattice contribution to thermal conductivity is therefore calculated as $4.3\ \mathrm{W\,m^{-1}\,K^{-1}}$. It should be noted that this method of extracting a cross-plane lattice thermal conductivity is reasonable since $Ti_{0.7}W_{0.3}N$ is an isotropic random alloy. Earlier results [25] showed that sputter deposited TiN thin films have a room temperature thermal conductivity of $63\ \mathrm{W\,m^{-1}\,K^{-1}}$, which suggests that incorporation of heavy tungsten (W) atoms in TiN reduces the overall thermal

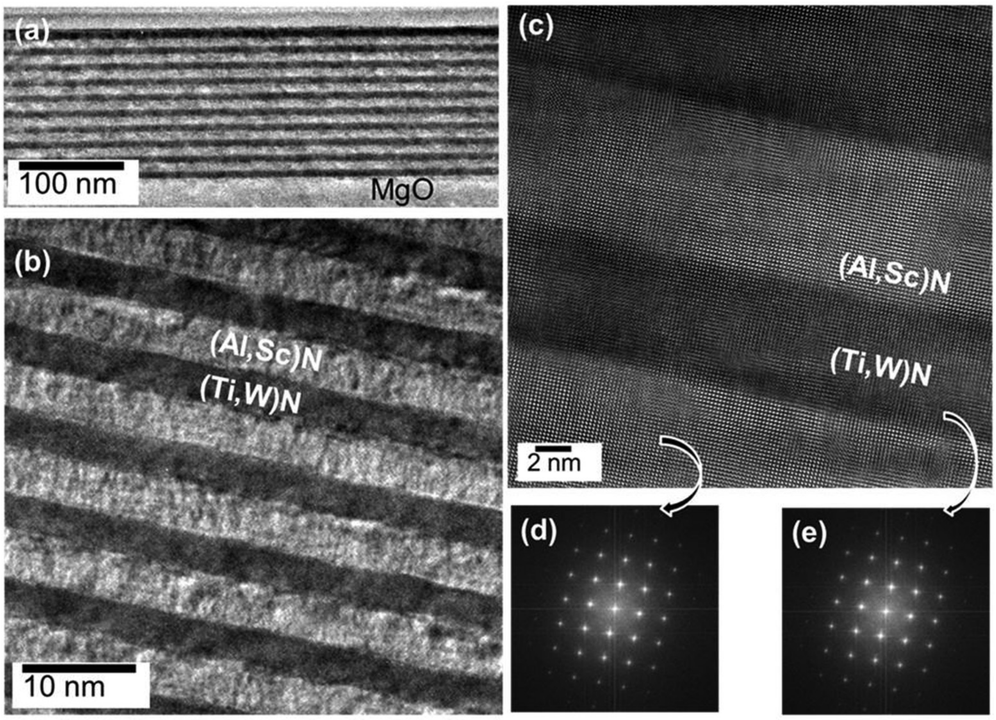

FIG. 2. (a) Low-magnification TEM image of a 5 nm/5 nm $Ti_{0.7}W_{0.3}N/Al_{0.72}Sc_{0.28}N$ superlattice grown on [001] MgO substrate. (b) Low-magnification TEM micrograph of the superlattice that shows $Ti_{0.7}W_{0.3}N$ and $Al_{0.72}Sc_{0.28}N$ layers separated by sharp and abrupt interfaces. (c) Atomic resolution TEM micrograph demonstrating the epitaxial nature of the crystal growth. (d), (e) FFTs from the $Al_{0.72}Sc_{0.28}N$ and $Ti_{0.7}W_{0.3}N$ layers, respectively, showing cubic diffraction patterns.

conductivity by one order of magnitude. The room temperature electrical conductivity of TiN was estimated [25] to be $1.5 \times 10^7\,S\,m^{-1}$, resulting in an electronic contribution to the thermal conductivity of $46\,W\,m^{-1}\,K^{-1}$. Heavy W atoms therefore affect the electrical conductivity of the alloy quite significantly.

The room temperature thermal conductivity of the $Al_{0.72}Sc_{0.28}N$ alloy is $4.5\,W\,m^{-1}\,K^{-1}$. The measured thermal conductivity is almost entirely due to the lattice (phonon) contribution since $Al_{0.72}Sc_{0.28}N$ is a semiconductor with high electrical resistivity (see Ref. [22]).

The cross-plane thermal conductivity of the $Ti_{0.7}W_{0.3}N/Al_{0.72}Sc_{0.28}N$ superlattices (Fig. 4) decreases from $4.5\,W\,m^{-1}\,K^{-1}$ to $1.7\,W\,m^{-1}\,K^{-1}$ as the superlattice period thickness decreases from 240 nm to 4 nm, respectively. The thermal conductivity then remains constant at $1.7\,W\,m^{-1}\,K^{-1}$ for period thicknesses of 4 nm, 3 nm, and 2 nm but increases to $2.6\,W\,m^{-1}\,K^{-1}$ at a period thickness of 1 nm. The thermal conductivity value of $1.7\,W\,m^{-1}\,K^{-1}$ for the 4 nm period tungsten-alloyed superlattice is about 2.5 times lower than a 4 nm period TiN/(Al,Sc)N superlattice ($4.5\,W\,m^{-1}\,K^{-1}$), demonstrating the beneficial effect of tungsten alloying. The decreasing thermal conductivity with decreasing superlattice period thickness (and concomitant increasing interface density) is due to incoherent phonon scattering at interfaces. Within the classical description of heat transport, each interface in a superlattice acts as a barrier for phonon transport, resulting in a boundary resistance that adds up in series. We kept the total superlattice thickness constant so that a decreasing period thickness results in an increasing number of interfaces, thereby increasing the total interface resistance and reducing the cross-plane thermal conductivity.

The saturation of thermal conductivity at $1.7\,W\,m^{-1}\,K^{-1}$ for short superlattice period thickness values (2 nm to 4 nm) cannot be attributed to any specific scattering mechanism. All incoherent scattering mechanisms, such as alloy scattering or interface scattering, will have a diminishing effect on the thermal conductivity as the density of scattering centers becomes sufficiently high. Therefore, we cannot quantitatively separate the role of coherent or incoherent scattering on the saturating thermal conductivity at small period thicknesses. However, we have previously described that phonon transport at such low period thicknesses in $TiN/Al_{0.72}Sc_{0.28}N$ superlattices involves wave effects due to the formation of phonon minibands and phonon zone folding [25,29]. At short superlattice periods, long-wavelength phonon [29] modes that do not interact with interfaces and that travel ballistically across the superlattice also play a significant role in thermal transport. In our description of heat transport in superlattices, we refer to both of these wave related mechanisms as long-wavelength coherent phonon modes because it is extremely difficult to separate them experimentally. In the case of TiN/(Al,Sc)N superlattices, the cross-plane thermal conductivity increases with decreasing period thickness below 4 nm primarily due to the long-wavelength coherent phonon modes. However, in the case of $Ti_{0.7}W_{0.3}N/Al_{0.72}Sc_{0.28}N$ superlattices, our results indicate that incoherent boundary scattering from interfaces and alloy scattering from the heavy tungsten atomic sites at short period thickness counterbalance the role of long-wavelength coherent phonon modes.

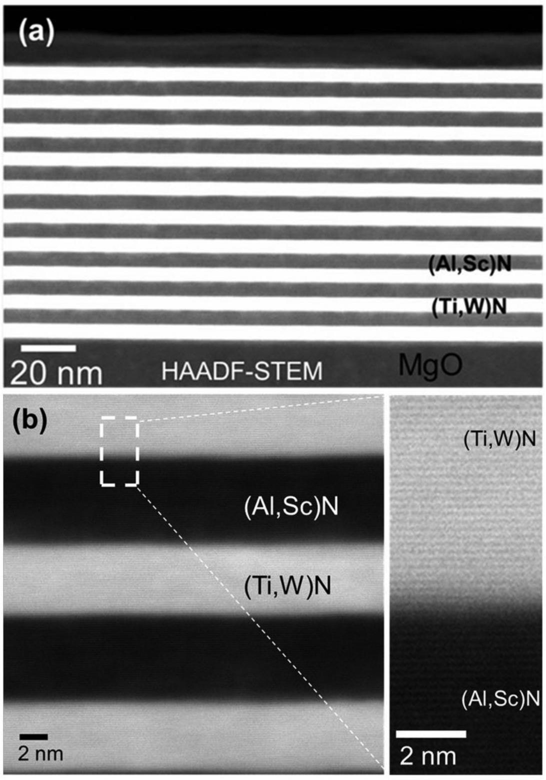

FIG. 3. (a) HAADF-STEM image of the $Ti_{0.7}W_{0.3}N/Al_{0.72}Sc_{0.28}N$ superlattice. The $Ti_{0.7}W_{0.3}N$ layers appear bright in the micrograph due to the (atomic number) Z-contrast producing method. (b) Sharp and abrupt interfaces are observed even at atomic resolution, demonstrating the high crystalline quality. The inset shows the lattice fringes.

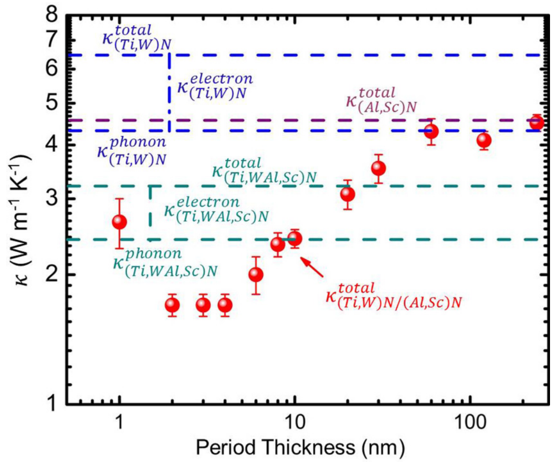

FIG. 4. Cross-plane thermal conductivity of the $Ti_{0.7}W_{0.3}N/Al_{0.72}Sc_{0.28}N$ superlattices as a function of period thickness. The thermal conductivity of the component materials and the alloys are presented as dashed lines along with their phonon contributions to the thermal conductivity. The superlattice thermal conductivity saturates at 1.7 W m^{-1} K^{-1} for low period superlattices.

Phonon transport in superlattices, just like in bulk materials, is a broadband phenomenon with characteristic mean free path values ranging from nanometers to micrometers. The modeling section and subsequent analysis will show that the long-wavelength coherent phonon modes play a significant role in heat transport across the entire investigated period thickness range in $Ti_{0.7}W_{0.3}N/Al_{0.72}Sc_{0.28}N$ superlattices. For long-period superlattices, these long-wavelength modes are overwhelmed by incoherent scattering at the boundaries, which results in decreasing thermal conductivity with increasing interface density. For short-period superlattices, the long-wavelength phonon modes become increasingly dominant, which probably causes the thermal conductivity to saturate. The increased thermal conductivity of the 1 nm period superlattice is probably due to intermixing at the interfaces due to the energetic sputtering process since the thermal conductivity is nearly the same as that of the $Ti_{0.35}W_{0.15}Al_{0.36}Sc_{0.14}N$ alloy. However, a substantial electronic contribution to the thermal conductivity due to tunneling electrical current cannot be ruled out for this superlattice.

We have also measured the room temperature cross-plane thermal conductivity of a $Ti_{0.35}W_{0.15}Al_{0.36}Sc_{0.14}N$ alloy since it represents the equivalent alloy composition of the $Ti_{0.7}W_{0.3}N/Al_{0.72}Sc_{0.28}N$ superlattices. The $Ti_{0.35}W_{0.15}Al_{0.36}Sc_{0.14}N$ alloy exhibits a room temperature thermal conductivity of 3.2 W m^{-1} K^{-1}, nearly half the value of the $Ti_{0.7}W_{0.3}N$ alloy. The calculated electronic contribution to thermal conductivity for the $Ti_{0.35}W_{0.15}Al_{0.36}Sc_{0.14}N$ alloy is 0.8 W m^{-1} K^{-1}, which means the lattice contribution to thermal conductivity is 2.4 W m^{-1} K^{-1}. The low thermal conductivity of the alloy is primarily due to lower group velocities of phonon modes as well as incoherent alloy scattering. Our room temperature results also show that the thermal conductivity of the short-period $Ti_{0.7}W_{0.3}N/Al_{0.72}Sc_{0.28}N$ superlattices is smaller than that of the lattice contribution to thermal conductivity of the $Ti_{0.35}W_{0.15}Al_{0.36}Sc_{0.14}N$ alloy. The alloy limit of thermal conductivity has traditionally represented the minimum achievable thermal conductivity in inorganic materials, but some researchers [12,30] have suggested that superlattices may overcome this traditional barrier. Therefore, in terms of basic scientific pursuits, our results are yet another demonstration of superlattices achieving thermal conductivity lower than the alloy limit. It is important to note that while the minimum thermal conductivity of TiN/(Al,Sc)N superlattice was obtained at 4 nm periods, its value was not lower than the equivalent alloy.

B. Temperature-dependent thermal conductivity

We measured the temperature-dependent cross-plane thermal conductivity of the superlattices and alloys in the 300 K to 500 K temperature range to understand details of the heat transport mechanisms. We also measured the temperature-dependent electrical conductivity of the $Ti_{0.7}W_{0.3}N$ and $Ti_{0.35}W_{0.15}Al_{0.36}Sc_{0.14}N$ alloy samples to determine the electronic contribution to the total thermal conductivity. Figure 5(a) shows the thermal conductivity of the $Ti_{0.7}W_{0.3}N$ alloy increasing from 6.5 to 10.8 W m^{-1} K^{-1} and the $Ti_{0.35}W_{0.15}Al_{0.36}Sc_{0.14}N$ alloy increasing from 2.8 to 5.4 W m^{-1} K^{-1} over the 300 K to 500 K temperature range. This behavior in the alloy samples is due to an increase in the electronic contribution to thermal conductivity associated with an increasing electrical conductivity. The electronic

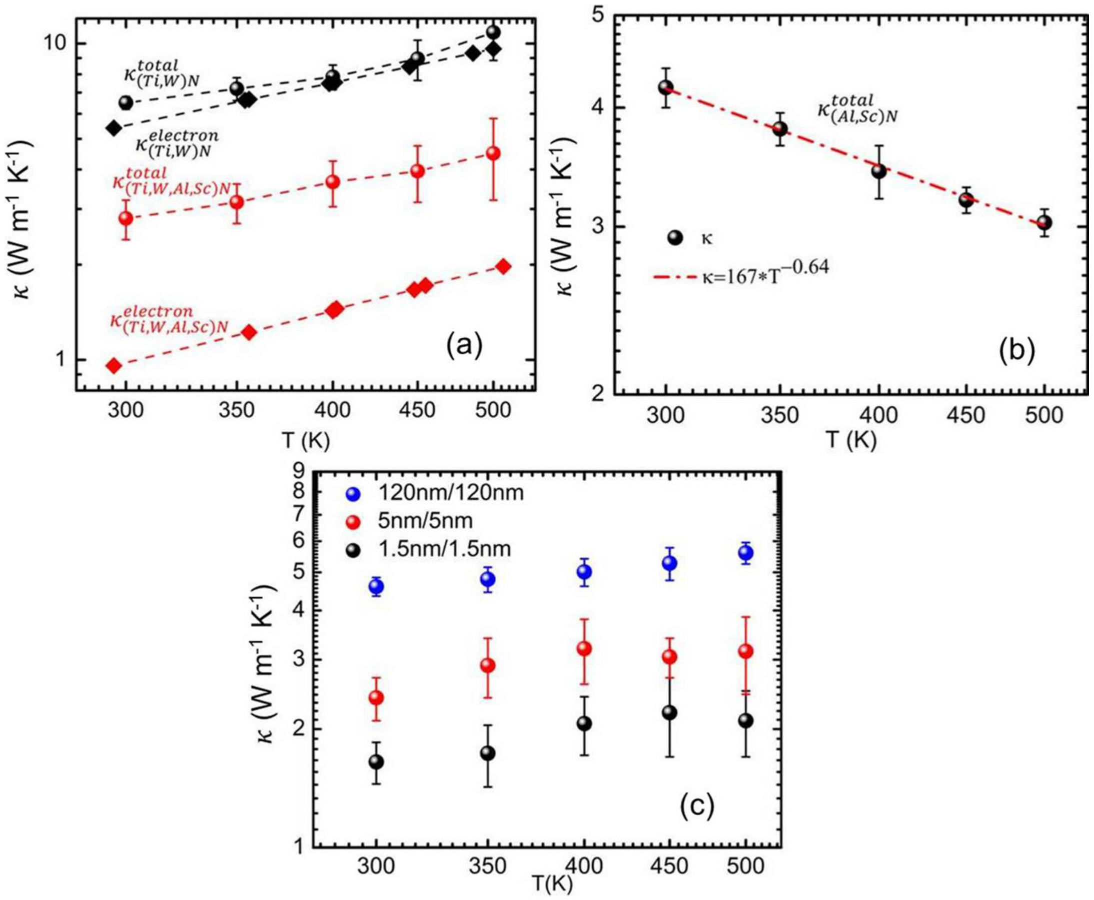

FIG. 5. Temperature-dependent cross-plane thermal conductivity of (a) $Ti_{0.7}W_{0.3}N$ and $Ti_{0.35}W_{0.15}Al_{0.36}Sc_{0.14}N$ alloy thin films (along with electron and phonon contributions). For $Ti_{0.7}W_{0.3}N$, the electronic contribution to thermal conductivity dominates the overall thermal conductivity, which is characteristic for a good metal. For $Ti_{0.35}W_{0.15}Al_{0.36}Sc_{0.14}N$, the electronic contribution to thermal conductivity is moderate. (b) The $Al_{0.72}Sc_{0.28}N$ film suggests a dominant anharmonic umklapp process at high temperatures. (c) The $Ti_{0.7}W_{0.3}N/Al_{0.72}Sc_{0.28}N$ superlattices with period thicknesses of 3 nm, 10 nm, and 240 nm. The thermal conductivity of the 240 nm period superlattice increases significantly (by 20%) with increasing temperature compared to the small period superlattices due to the trapped electrons in the thick $Ti_{0.7}W_{0.3}N$ layers.

contribution to thermal conductivity accounts for 85–90% of κ_{total} for the $Ti_{0.7}W_{0.3}N$ alloy and 33–40% of κ_{total} for the $Ti_{0.35}W_{0.15}Al_{0.36}Sc_{0.14}N$ alloy over the measured temperature range. Increasing electrical conductivity as a function of temperature is not typical for metallic alloys and may be related to trapped electrons due to incorporation of tungsten nitride (WN) in the TiN matrix. These trapped electrons are not mobile at room temperature, but they can overcome the energy activation barrier and contribute to electrical conduction as the temperature is increased. Therefore, we see an increase in the total thermal conductivity of the alloy samples with increasing temperature. The nature of the electrical conductivity vs temperature data [see Fig. 5(a)] also suggests that there must be multiple activation barriers of different barrier heights that lead to an effective linear increase in conductivity with respect to increasing temperatures. The increasing electronic contribution to thermal conductivity also reduces the relative importance of anharmonicity that usually dominates thermal transport at high temperatures. On the other hand, the $Al_{0.72}Sc_{0.28}N$ alloy behaves as expected with the thermal conductivity decreasing as a function of temperature due to umklapp scattering [Fig. 5(b)]. The umklapp scattering exponent for $Al_{0.72}Sc_{0.28}N$ was determined to be 0.65, a typical value for an alloy sample.

Figure 5(c) shows the temperature-dependent thermal conductivity results for three superlattices with period thickness values of 3 nm, 10 nm, and 240 nm, whereby each period thickness represents a different regime of phonon transport. The thermal conductivity of the 240 nm period superlattice (i.e., only one period) increases by ~20% from 300 K to 500 K—expected behavior given that half of the total thickness (120 nm) is contributed by $Ti_{0.7}W_{0.3}N$. The thermal conductivities of the 3 nm and 10 nm period superlattices increase by ~25% and ~30%, respectively, from 300 K to 400 K, but saturate from 400 K to 500 K. The overall thermal conductivity of the short-period superlattices does not follow the same trend as in the case of the 240 nm period bilayer due to the thinner $Ti_{0.7}W_{0.3}N$ layers. However, a significant electronic contribution to thermal conductivity is still present in the short-period superlattices at high temperature. Otherwise the thermal conductivity would have decreased significantly due to anharmonic umklapp scattering.

C. Interface thermal conductance

The ITC values are conventionally used to explain thermal transport in single heterojunctions where the component materials are effectively infinitely thick in both directions. In the case of a superlattice, estimates of the ITC are only relevant in the incoherent transport regime. However, even in the incoherent transport regime, superlattices (especially with short periods) support long-wavelength coherent phonon modes that do not see interfaces and contribute significantly to the thermal conduction. Therefore, estimates of ITC from experimental measurements and their comparisons with traditional theoretical models (e.g., acoustic mismatch model (AMM), diffuse mismatch model (DMM) with Debye frequency, and DMM with full phonon dispersions) might reveal significant details about the transport mechanisms. However, caution must be exercised when drawing conclusions from these models since all three theoretical models mentioned above are defined for single heterojunctions of bulk materials (see the Supplemental Material [26] for details).

We estimate the room temperature ITC between $Ti_{0.7}W_{0.3}N$ and $Al_{0.72}Sc_{0.28}N$ layers in the superlattice only in the incoherent phonon transport regime. The total superlattice resistance is written as a summation of the resistance from individual layers as well as from the interfaces in Eq. (1):

$$R_{\text{superlattice}} = R_{(\text{Ti,W})\text{N}} + R_{(\text{Al,Sc})\text{N}} + R_{\text{interface}}. \tag{1}$$

When expressed in terms of boundary resistance (R_B) that is the reciprocal of ITC, number of interfaces (N), and the total superlattice thickness (L), Eq. (1) becomes

$$\frac{NR_B}{L} = \frac{1}{\kappa_{\text{superlattice}}} - \frac{1}{2}\left(\frac{1}{\kappa_{(\text{Ti,W})\text{N}}} + \frac{1}{\kappa_{(\text{Al,Sc})\text{N}}}\right). \tag{2}$$

However, we see that to estimate the ITC from Eq. (2), the thermal conductivities of the $Ti_{0.7}W_{0.3}N$ and $Al_{0.72}Sc_{0.28}N$ layers are required when their thicknesses are exactly half of the period thicknesses. Since the period thicknesses of most of the superlattices are very small, they do not possess sufficient resistance to be measured with an experimental technique. We calculate ITC values using two different scenarios for the thermal conductivity of the layers. Scenario (a) assumes that the thermal conductivity of the individual layers in the superlattice (irrespective of their thicknesses) is equivalent to the measured thermal conductivity of a 240 nm thin film. In other words, $\kappa^{\text{for all thicknesses}}_{(\text{Ti,W})\text{N}} = \kappa^{240\text{ nm}}_{(\text{Ti,W})\text{N}} = 6.3\text{ W m}^{-1}\text{ K}^{-1}$, and $\kappa^{\text{for all thickness}}_{(\text{Al,SC})\text{N}} = \kappa^{240\text{ nm}}_{(\text{Al,Sc})\text{N}} = 4.5\text{ W m}^{-1}\text{ K}^{-1}$. Therefore, Eq. (2) for scenario (a) takes the form,

$$\frac{NR_B}{L} = \frac{1}{\kappa_{\text{superlattice}}} - \frac{1}{2}\left(\frac{1}{6.3} + \frac{1}{4.5}\right). \tag{3}$$

This assumption implies that phonon scattering is diffusive within an individual layer even though its thickness might be small, which should be true when the layer thickness is larger than the phonon mean free path. Scenario (b) assumes that phonons travel ballistically (i.e., no resistance) through the individual layers such that the entire resistance of the superlattices is assumed to be at the interfaces. The thermal resistances of the individual layers are negligible, which should be reasonable for short-period superlattices when the layer thicknesses are sufficiently smaller than the phonon mean free path. The calculated ITC in scenario (b) should represent the lowest possible ITC values. Equation (2) for scenario (b), therefore, takes the form

$$\frac{NR_B}{L} = \frac{1}{\kappa_{\text{superlattice}}}. \tag{4}$$

The ITC calculated with these two assumptions is presented as a function of the period thickness in Fig. 6(a). For scenario (a), the room temperature ITC for a 30 nm $Ti_{0.7}W_{0.3}N$/30 nm $Al_{0.72}Sc_{0.28}N$ interface (i.e., only one interface) is estimated to be $0.66\text{ GW m}^{-2}\text{ K}^{-1}$, representing the single-heterojunction ITC limit with which traditional modeling results can be compared (note that the thermal conductivity saturates for larger period thicknesses). It is clear from Fig. 6(a) that the room temperature ITC increases steadily as the period thickness decreases. For a 30 nm/30 nm, 20 nm/20 nm, and 2 nm/2 nm superlattice, the ITC values are $0.66\text{ GW m}^{-2}\text{ K}^{-1}$, $0.70\text{ GW m}^{-2}\text{ K}^{-1}$, and $1.24\text{ GW m}^{-2}\text{ K}^{-1}$, respectively. The

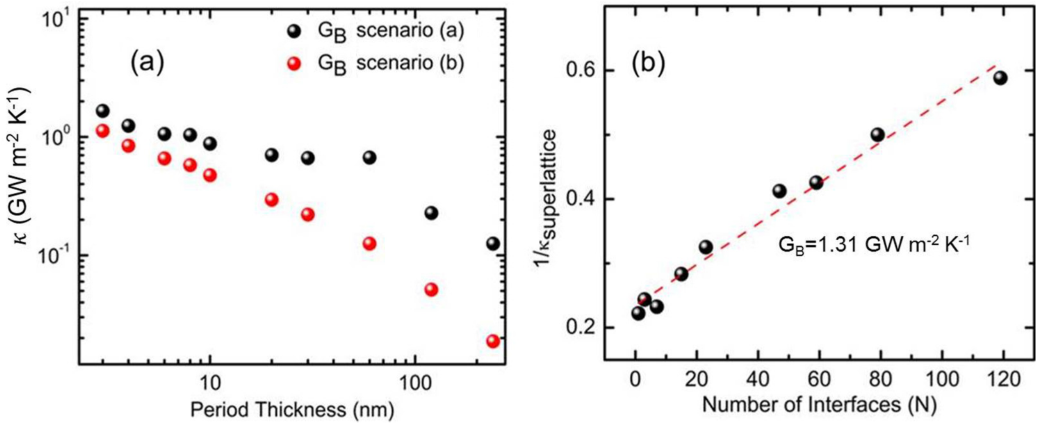

FIG. 6. (a) ITC values of $Ti_{0.7}W_{0.3}N/Al_{0.72}Sc_{0.28}N$ superlattices as a function of the superlattice period thicknesses. The ITCs are calculated from experimental results using two assumptions. Scenario (a) assumes that the thermal conductivity of the individual layers are the same as the thermal conductivity of an equivalent 240 nm thin film, while scenario (b) assumes that all the resistance originates from the interfaces. (b) Average ITC extracted from a plot of $\frac{1}{\kappa_{\text{superlattice}}}$ as a function of the number of interfaces in the superlattice. This method does not require any assumptions about the thermal conductivity of the individual layers.

observed ITC vs period thickness behavior is due to long-wavelength coherent phonon modes. The minimum wavelength of the phonon mode must be at least the same as the superlattice period thickness in order to overcome incoherent scattering (i.e., phonon does not see interface). The contribution of long-wavelength coherent phonon modes to thermal transport increases as the period thickness decreases, resulting in increasing ITC values. The 4 nm period superlattice has a room temperature ITC 10 times greater than that of the 240 nm period thickness, which suggests that the contribution of long-wavelength coherent phonon modes to thermal conduction increases with reduction in period thickness of the superlattices. Our results are consistent with our previous observations where long-wavelength coherent phonon modes contributed about 83% of the total thermal conduction in short-period TiN/(Al,Sc)N superlattices. Our results are also consistent with the theoretical calculation of Luckyanova *et al.* [4], which predicts that 86% of heat in the superlattice is carried by long-wavelength coherent phonon modes in GaAs/AlAs superlattices.

Similar to the results of scenario (a), scenario (b) shows an increasing room temperature ITC with decreasing period thickness [Fig. 6(a)]. Scenario (b) is expected to work best for short-period superlattices. The ITC of a 4 nm period superlattice is 1.12 W $\mathrm{m}^{-2}\,\mathrm{K}^{-1}$, which is close to the ITC value calculated under scenario (a). However, the ITC data from scenario (a) and scenario (b) diverge with increasing period thickness. Estimated ITC values for long-period superlattices are much smaller for scenario (b) than the results obtained for scenario (a) since scenario (b) neglects a significant portion of the thermal resistance emanating from the individual layers.

The methods described above require knowledge of the thermal conductivity of the individual materials with very small thicknesses, data that are hard to obtain experimentally. Therefore, we have employed a third method for estimating ITC that does not require the thermal conductivity of the individual layers. We use Eq. (2) to plot a linear curve between $\frac{1}{\kappa_{\mathrm{superlattice}}}$ vs N and the slope of the curve is used to estimate the ITC. However, it is not possible to estimate the ITC as a function of period thickness with this technique; rather, we get a single averaged value. The average room temperature ITC is determined to be 1.31 GW $\mathrm{m}^{-2}\,\mathrm{K}^{-1}$, which is similar to the ITC value from scenario (a). The ITC values estimated here are about four times smaller than the ITC values measured for TiN/(Al,Sc)N superlattices, which underlines the role of tungsten atoms in decreasing the cross-plane thermal conductivity and ITC values of $\mathrm{Ti}_{0.7}\mathrm{W}_{0.3}\mathrm{N}/\mathrm{Al}_{0.72}\mathrm{Sc}_{0.28}\mathrm{N}$ superlattices. It is also important to note that a single average thermal interface resistance can explain the superlattice interface number dependence from 1 nm to 240 nm. However, the TiN/(Al,Sc)N superlattices show at least three regimes where ITC changes by a factor of about five between small number of superlattice interfaces and a large number of interfaces.

D. Modeling vibrational spectra and ITC

Theoretical models like AMM and DMM require phonon group velocities and Debye temperatures of the individual materials to predict the ITC. However, $\mathrm{Ti}_{0.7}\mathrm{W}_{0.3}\mathrm{N}$ and $\mathrm{Al}_{0.72}\mathrm{Sc}_{0.28}\mathrm{N}$ alloys are developed solely for our purpose and, to our knowledge, there are no literature results of their physical properties. Therefore, we employ first-principles density functional perturbation theory (DFPT) based simulations to calculate the vibrational spectra of both (Ti,W)N and (Al,Sc)N and use the results to estimate the ITC. Details about the method of DFPT calculations are presented in the Supplemental Material [26]. It is important to note that we used slightly different concentrations of the individual materials in order to optimize computational resources and time [i.e., 75% instead of 70% Ti in (Ti,W)N and 75% instead of 72% Al in (Al,Sc)N]. These small concentration changes allow us to model an eight atom unit cell with a 3:1 Ti:W ratio and an eight atom unit cell with a 3:1 Al:Sc ratio with much less computational resources. It is also important to note that these DFPT calculations for the constituent materials are performed with ordered alloy configurations to save computational time and resources. Thin films grown in this study are, however, random alloys. This difference between simulations and experiments is not expected to affect our qualitative explanations, but caution must be exercised in the quantitative comparisons with experimental results.

The phonon dispersion spectrum [Fig. 6(a)] suggests that both the longitudinal acoustic (LA) and the transverse acoustic (TA) phonon modes soften in $\mathrm{Ti}_{0.75}\mathrm{W}_{0.25}\mathrm{N}$ compared to TiN [see the Γ-X direction in Fig. 7(a)] due to the heavy tungsten (W) atoms that vibrate with smaller frequencies. It is also clear from the dispersion spectrum that group velocities of TA phonon modes are significantly smaller than that of the LA mode and increase only very slightly as we move along Γ-X directions of the Brillouin zone. Such small phonon frequencies and flat phonon bands lead to smaller phonon group velocities resulting in lower lattice thermal conductivity of $\mathrm{Ti}_{0.75}\mathrm{W}_{0.25}\mathrm{N}$ (6.25 W $\mathrm{m}^{-1}\,\mathrm{K}^{-1}$ at room temperature). In our experiment, we have observed a 10-fold reduction in the thermal conductivity of $\mathrm{Ti}_{0.75}\mathrm{W}_{0.25}\mathrm{N}$ with respect to TiN; the softening of the acoustic phonon frequencies is one of the main reasons for such a decrease in thermal conductivity. It should also be kept in mind that some portion of the thermal conductivity reduction is also due to the alloy scattering effects. The acoustic phonon branches of $\mathrm{Ti}_{0.75}\mathrm{W}_{0.25}\mathrm{N}$ range from 0 to 120 cm^{-1}, while in TiN they range from 0 to 300 cm^{-1}. The optical phonon branches having frequencies 450 to 650 cm^{-1} in $\mathrm{Ti}_{0.75}\mathrm{W}_{0.25}\mathrm{N}$ represent nitrogen atomic vibrations since nitrogen is the lighter atom that vibrates with higher frequencies. The dispersion spectra also suggest that there is some mixing between the acoustic and optical phonon modes, and there exists a gap in the dispersion spectra ranging from 300 to 450 cm^{-1} where no vibrational states are present. Unlike other transition metal nitrides (like HfN, ZrN, and, to some extent, TiN), the $\mathrm{Ti}_{0.75}\mathrm{W}_{0.25}\mathrm{N}$ alloy does not show any anomaly in the phonon dispersion spectrum.

The phonon dispersion of $\mathrm{Al}_{0.75}\mathrm{Sc}_{0.25}\mathrm{N}$ is presented in Fig. 7(b), and the spectrum suggests that both LA and TA phonon modes are much steeper compared to $\mathrm{Ti}_{0.75}\mathrm{W}_{0.25}\mathrm{N}$. The acoustic phonon branches in $\mathrm{Al}_{0.75}\mathrm{Sc}_{0.25}\mathrm{N}$ range from 0 to 275 cm^{-1}, higher than $\mathrm{Ti}_{0.75}\mathrm{W}_{0.25}\mathrm{N}$, and there is significant mixing of its acoustic and optical phonon modes. Unlike $\mathrm{Ti}_{0.75}\mathrm{W}_{0.25}\mathrm{N}$, there is no gap in the phonon dispersion spectrum of $\mathrm{Al}_{0.75}\mathrm{Sc}_{0.25}\mathrm{N}$. Our calculations suggest that the dielectric constant $\varepsilon(\infty)$ of $\mathrm{Al}_{0.75}\mathrm{Sc}_{0.25}\mathrm{N}$ is 6.54. Though

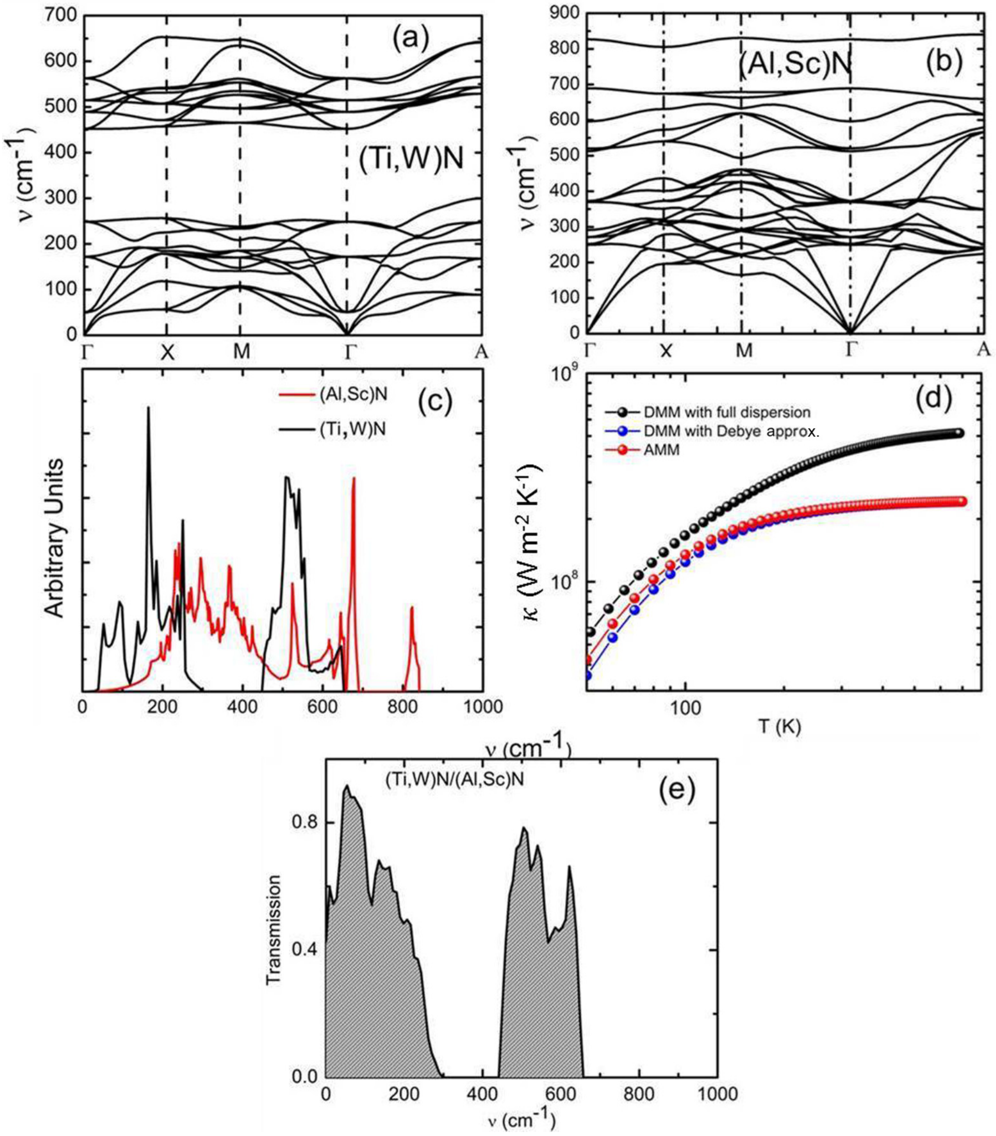

FIG. 7. (a) Vibrational spectra of (Ti,W)N alloy is presented along the high symmetry direction of the Brillouin zone. Acoustic phonon branches are much softer in (Ti,W)N compared to TiN. (b) Vibrational spectra of (Al,Sc)N alloy along the high symmetry directions of the Brillouin zone. Acoustic branches have higher phonon group velocities. (c) Densities of the vibrational states of the (Ti,W)N and (Al,Sc)N layers are presented. The figure suggests that there is significant mismatch in the vibrational spectra of the component materials. (d) Theoretical calculations of the interface thermal conductance (ITC) are presented as a function of temperatures. The ITCs are calculated with DMM with Debye approximation, DMM with full Brillouin zone dispersions, and AMM. (e) Phonon transmission spectrum across the (Ti,W)N/(Al,Sc)N interface calculated from the DMM analysis is presented as a function of the phonon frequencies.

DFPT usually overestimates the dielectric constant of semiconductors, our modeling results match very well with our experimental dielectric constant measurement for the $Al_{0.75}Sc_{0.25}N$ alloy (see Refs. [22] and [23] for details).

The phonon densities of states (DOS) [presented in Fig. 6(c)] reveal significant information about the transport mechanism across the interfaces. Figure 7(c) suggests noticeable mismatch in the phonon DOS between the two materials. $Ti_{0.75}W_{0.25}N$ has a large number of high velocity acoustic and optical phonon modes in the 25–250 cm^{-1} frequency ranges. However, within the same frequency range, there are a much smaller number of phonon modes for $Al_{0.75}Sc_{0.25}N$. This mismatch in the densities of high velocity phonon states will significantly reduce the ITC across the $Ti_{0.75}W_{0.25}N/Al_{0.75}Sc_{0.25}N$ interface, as we shall see later in the transport models. Another significant difference between the phonon DOS of the two materials is the absence of any $Ti_{0.75}W_{0.25}N$ phonon modes in the 300 to 450 cm^{-1} frequency ranges where a large number of $Al_{0.75}Sc_{0.25}N$ phonon modes is present. Such mismatch in the dispersion spectra should generate phonon stop bands with very low transmission probabilities across the interface, which should also reduce the ITC.

Debye temperatures of the materials are extracted from the calculated dispersion spectra. We find that the Debye temperature of $Ti_{0.75}W_{0.25}N$ is about 373 K, while for $Al_{0.75}Sc_{0.25}N$ it is 570 K. Such a large difference (∼200 K) in the Debye temperature of the component materials is due to the difference in the velocities of the acoustic phonon modes.

The ITC calculated with AMM, DMM with Debye dispersion, and DMM that employs full phonon dispersion [presented in Fig. 7(d)] suggest that at room temperature both the AMM and the DMM with the Debye approximation predict an ITC of 0.22 GW m^{-2} K^{-1} across the $Ti_{0.75}W_{0.25}N/Al_{0.75}Sc_{0.25}N$ interface. Our experimental analyses have suggested that the ITC for a 120 nm/120 nm interface is 0.12 GW m^{-2} K^{-1}; therefore, the calculated ITC matches reasonably well with the experimental observations. For most inorganic hetero-interfaces, AMM and DMM generally overestimate the ITC since real interfaces almost always have disorder that reduces transmission probabilities. Therefore, our modeling results agree reasonably well with the experimental results. However, the DMM calculation that uses full Brillouin zone phonon dispersion predicts that the ITC across the interface is about 0.41 GW m^{-2} K^{-1}, which is twice that of the normal DMM calculation. Careful observation of the transmission function calculated with DMM analysis [presented in Fig. 7(e)] suggests that some optical modes, which are neglected in the DMM analysis with the Debye approximation analysis, have relatively larger group velocities and that they contribute significantly to the phonon thermal conductance across the superlattice interface.

In our modeling analysis, we have not incorporated the electronic contribution to the interface thermal boundary resistance and thermal conductivity. In metal/semiconductor superlattices, cross-plane electrical transport is governed by the Schottky barrier height. If the barrier height is small (of the order of kT), a significant amount of current may result across the interface at room temperature, leading to an appreciable electronic contribution to thermal conductivity. On the other hand, if the barrier height is large ($>kT$), current across the interface would be negligible. Though we do not have a direct estimate of the barrier height in (Ti,W)N/(Al,Sc)N superlattices, from our experience in previous studies on TiN/(Al,Sc)N, HfN/ScN and ZrN/ScN metal/semiconductor superlattices, we anticipate that the barrier height across the (Ti,W)N/(Al,Sc)N interface would be large and there would not be appreciable electrical current across the interface at room temperature. Therefore, thermal transport in these nitride superlattices is likely to be primarily governed by lattice contributions or phonons at room temperatures, and it is safe to neglect the electronic contribution to the thermal conductivity at room temperatures.

E. Modeling alloy scattering

To explain the suppression of coherent effects in (Ti,W)N/(Al,Sc)N superlattice, we have performed a theoretical analysis of alloy scattering in $Ti_{0.7}W_{0.3}N$ and $Al_{0.72}Sc_{0.28}N$ systems. Alloy scattering has been modeled in prior literature in a manner similar to point defect scattering of phonons in a virtual crystal [31]. We adopt a similar approach here to estimate the relative effects of W atoms on the phonons of TiN as well as Sc atoms on phonons in AlN respectively. The scattering rate due to substitutional impurities or point defects was derived by Klemens [32] to have the following dependence on phonon frequency:

$$\tau_i^{-1} = \frac{\omega^4 V \Gamma_i}{4\pi v^3},$$

where V is the unit cell volume, v is the phonon group velocity, and Γ_i is a measure of the scattering cross-section of the impurity atom. Γ_i contains terms due to mass mismatch, change in the local atomic volume, and change in the local interatomic force constants. To obtain an approximate estimate of the scattering time, we consider only the effect of mass mismatch on Γ_i, as the change in other parameters is not well known and their effects cancel each other.

The parameter Γ is defined as

$$\Gamma_i = \sum_i c_i \left(\frac{m_i - \bar{m}}{\bar{m}}\right)^2,$$

where c_i is the concentration of the impurity atom of mass m_i. In the $Ti_{0.7}W_{0.3}N$ alloy, we consider W atoms as substitutional impurities on Ti atomic sites to calculate the scattering cross-section Γ. Similarly for $Al_{0.72}Sc_{0.28}N$, we consider Sc atoms as point impurities in Al atomic sites. The value of Γ for W impurities on TiN is 0.49, while that for Sc impurities on AlN is 0.06. Hence, the scattering cross-section for W alloy scattering in (Ti,W)N is about 100 times more than that for Sc atoms in (Al,Sc)N. Substituting for the unit cell volumes of TiN and AlN along with their group velocities (averaged over LA and TA modes), we obtain a ratio in alloy scattering rates of TiN and AlN to be approximately 30.

Although (Ti,W)N and (Al,Sc)N are both alloy materials, the mean free path of phonons in (Ti,W)N is expected to be significantly smaller than the mean free path in (Al,Sc)N due to the large scattering cross-section of W atoms. This is likely the reason that coherent effects that manifest in the TiN/(Al,Sc)N superlattice are suppressed in the (Ti,W)N/(Al,Sc)N superlattice.

IV. CONCLUSIONS

We have presented a detailed analysis of the growth, characterization, and cross-plane thermal transport properties of $Ti_{0.7}W_{0.3}N/Al_{0.72}Sc_{0.28}N$ metal/semiconductor superlattices with a motivation to design efficient thermoelectric materials.

(1) Epitaxial, nominally single crystalline $Ti_{0.7}W_{0.3}N/Al_{0.72}Sc_{0.28}N$ metal/semiconductor superlattices are sputter-deposited on 001 MgO substrates. The superlattices grow with 002 orientation, are pseudomorphic with respect to the MgO substrates, and exhibit low densities of extended defects. TEM clearly shows sharp and distinct superlattice interfaces and cubic epitaxial crystal growth.

(2) The room temperature cross-plane thermal conductivity for short-period superlattices (1.7 W m^{-1} K^{-1}) is well below the alloy limit, which makes them suitable for thermoelectric and thermionic applications from the standpoint of thermal transport. The lowest thermal conductivity of (Ti,W)N/(Al,Sc)N superlattices is achieved over a wider range of superlattice periods (2 nm to 4 nm) compared to that of TiN/(Al,Sc)N superlattices where the minimum thermal conductivity occurs at a period of 4 nm.

(3) Long-wavelength coherent phonon modes due to phonon wave effects that typically dominate thermal transport in short-period superlattices are counterbalanced by incoherent interface and alloy scattering, which leads to saturation of

thermal conductivity in short-period superlattices. Incorporation of WN in the TiN matrix helps enhance the incoherent scattering cross-sections, thereby reducing the thermal conductivity.

(4) Theoretical estimates of ITC for long-period superlattices (one period 120 nm $Ti_{0.7}W_{0.3}N$/120 nm $Al_{0.72}Sc_{0.28}N$ bilayer) match reasonably well with our experimental observations. A single average thermal interface resistance can explain the superlattice interface number dependence from 1 nm to 240 nm. On the other hand, TiN/AlScN superlattices showed at least three regimes where interface thermal resistance changes by 5× between a small number of superlattice interfaces and a large number of interfaces.

An in-depth and detailed thermal transport study of $Ti_{0.7}W_{0.3}N/Al_{0.72}Sc_{0.28}N$ metal/semiconductor superlattices presented here addresses some fundamental questions of heat transport mechanisms in superlattices. We show that it is possible to engineer heat transport in a metal/semiconductor superlattice to achieve a desired functionality, and the findings of this paper can be extended to other practical superlattice metamaterials.

ACKNOWLEDGMENTS

B.S. and T.D.S. acknowledge financial support from the National Science Foundation and U.S. Department of Energy (Award No. CBET-1048616). Y.K. and A.S. acknowledge financial support from the Defense Advanced Research Projects Agency (DARPA)/Army Research Office, Contract No. W911NF0810347. J.C. thanks the Louis Stokes Alliance for Minority Participation (LSAMP) program for supporting his undergraduate research. The Knut and Alice Wallenberg (KAW) Foundation is acknowledged for the Electron Microscope Laboratory in Linköping. S.S. thanks funding support from the Office of Naval Research (Award No. N000141211006). B.S., J.L.S., M.G., J.B., and T.D.S. acknowledge financial support from the Swedish Research Council [RÅC Frame Program (2011-6505) and Linnaeus Grant (LiLi-NFM)] as well as the Swedish Government Strategic Research Area in Materials Science on Functional Materials at Linköping University (Faculty Grant SFO-Mat-LiU 2009-00971). B.S. and Y.K. thank Dr. Je-Hyeong Bahk for helping with aluminum depositions.

---

[1] D. G. Cahill, W. K. Ford, K. E. Goodson, G. D. Mahan, A. Majumdar, H. J. Maris, R. Merlin, and S. R. Phillpot, J. Appl. Phys. **93**, 793 (2003).

[2] W. Kim, R. Wang, and A. Majumdar, Nanotoday **2**, 40 (2007).

[3] D. G. Cahill, K. E. Goodson, and A. Majumdar, J. Heat Transfer **124**, 223 (2002).

[4] M. N. Luckyanova, J. Garg, K. Esfarjani, A. Jandl, M. T. Bulsara, A. J. Schmidt, A. J. Minnich, S. Chen, M. S. Dresselhaus, Z. Ren, E. Fitzgerald, and G. Chen, Science **338**, 936 (2012).

[5] J. Ravichandran, A. K. Yadav, R. Cheaito, P. B. Rossen, A. Soukiassian, S. J. Suresha, J. C. Duda, B. M. Foley, C. Lee, Y. Zhu, A. W. Lichtenberger, J. E. Moore, D. A. Muller, D. G. Schlom, P. E. Hopkins, A. Majumdar, R. Ramesh, and M. A. Zurbuchen, Nat. Mater. **13**, 168 (2014).

[6] A. Shakouri, Annu. Rev. Mater. Res. **41**, 399 (2011).

[7] C. J. Vineis, A. Shakouri, A. Majumdar, and M. G. Kanatzidis, Adv. Mater. **22**, 3970 (2010).

[8] D. Clarke, M. Oechsner, and N. P. Padture, MRS Bulletin **37**, 891 (2012).

[9] S. T. Huxtable, A. R. Abramson, C.-L. Tien, A. Majumdar, C. LaBounty, X. Fan, G. Zeng, J. E. Bowers, A. Shakouri, and E. T. Croke, Appl. Phys. Lett. **80**, 1737 (2002).

[10] V. Narayanamurti, H. L. Störmer, M. A. Chin, A. C. Gossard, and W. Wiegmann, Phys. Rev. Lett. **43**, 2012 (1979).

[11] S. M. Lee, D. G. Cahill, and R. Venkatasubramanian, Appl. Phys. Lett. **70**, 2957 (1997).

[12] R. Venkatasubramanian, Phys. Rev. B **61**, 3091 (2000).

[13] E. T. Swartz and R. O. Pohl, Rev. Mod. Phys. **61**, 605 (1989).

[14] G. Chen, Phys. Rev. B **57**, 14958 (1998).

[15] M. V. Simkin and G. D. Mahan, Phys. Rev. Lett. **84**, 927 (2000).

[16] A. Shakouri and J. E. Bowers, Appl. Phys. Lett. **71**, 1234 (1997).

[17] D. Vashaee and A. Shakouri, Phys. Rev. Lett. **92**, 106103 (2004).

[18] G. Chen and M. Neagu, Appl. Phys. Lett. **71**, 2761 (1997).

[19] B. Saha, T. D. Sands, and U. V. Waghmare, J. Appl. Phys. **109**, 083717 (2011).

[20] V. Rawat, Y. K. Koh, D. G. Cahill, and T. D. Sands, J. Appl. Phys. **105**, 024909 (2009).

[21] B. Saha, T. D. Sands, and U. V. Waghmare, J. Phys.: Condens. Matter **24**, 415303 (2012).

[22] B. Saha, S. Saber, G. V. Naik, A. Boltasseva, E. Stach, E. P. Kvam, and T. D. Sands, Phys. Stat. Sol. B **252**, 251 (2015).

[23] B. Saha, G. V. Naik, S. Saber, C. Akatay, E. A. Stach, V. M. Shalaev, A. Boltasseva, and T. D. Sands, Phys. Rev. B **90**, 125420 (2014).

[24] G. V. Naik, B. Saha, J. Liu, S. M. Saber, E. Stach, J. M. K. Irudayaraj, T. D. Sands, V. M. Shalaev, and A. Boltasseva, Proc. Natl. Acad. Sci. USA **111**, 7546 (2014).

[25] B. Saha, Y. R. Koh, S. Sadasivam, J. P. Feser, D. Cahill, A. Shakouri, T. S. Fisher, and T. D. Sands (unpublished).

[26] See Supplemental Material at http://link.aps.org/supplemental/10.1103/PhysRevB.93.045311 for the details about growth technique, XRD, HRTEM characterization, density functional theory based calculation method and interface conductance calculation, and details about TDTR measurements and data fitting.

[27] F. Tian, J. Gall, T. Y. Lee, M. Sardela, D. Gall, I. Petrov, and J. E. Greene, J. Vac. Sci. Technol. A: Vacuum, Surfaces, and Films **21**(1), 140 (2003).

[28] J. H. Moser, F. Tian, O. Haller, D. B. Bergstrom, I. Petrov, J. E. Greene, and C. Wiemer, Thin Solid Films **253**, 445 (1994).

[29] Y. K. Koh, Y. Cao, D. Cahill, and D. Jena, Adv. Fun. Matter **19**, 610 (2009).

[30] W. S. Capinski, H. J. Maris, T. Ruf, M. Cardona, K. Ploog, and D. S. Katzer, Phys. Rev. B **59**, 8105 (1999).

[31] J. Garg, N. Bonini, B. Kozinsky, and N. Marzari, Phys. Rev. Lett. **106**, 045901 (2011).

[32] P. G. Klemens, Proc. Phys. Soc. (London) A **68**, 1113 (1955).